Sandwich and Interdigitated Finger Electrode Ferroelectric Nano Film Capacitors: A Comparison of the Effect of Electrostatic Boundary Conditions and Defects

I. B. Misirlioglu*, M. Yildiz

Faculty of Engineering and Natural Sciences, Sabanci University, Tuzla/Orhanli, 34956 Istanbul, Turkey

Abstract

We compare the effect of electrostatic boundary conditions and defects on the electrical properties of epitaxial nano ferroelectric thin film capacitors with various electrode configurations. The capacitor geometries studied are parallel plate, or so called sandwich type electrodes and the interdigitated finger electrodes grown on the ferroelectric film. The defects, when present, are frozen-in dipoles of the *p*-type. The Landau-Ginzburg-Devonshire free energy coupled with the elastic and electrostatic boundary conditions is used to compute the electrical properties. A switchable ferroelectric polarization lying in the plane of the film for the case of interdigitated electrodes is weakly impacted by the presence of dead layers and asymmetrically distributed defects compared to a classical sandwich type nano film. An out of plane remanent polarization in a sandwich type capacitor, stabilized via compressive in-plane misfit, always forms in a multidomain configuration in ultrathin films with thin dead layers. An in-plane polarization stabilized by a tensile misfit, on the other hand, could be much more effectively used in memory device applications where interdigitated electrodes are possible to utilize. The latter also does not suffer as much from the possible presence of dead layers even in ultrathin structures (Film thickness < 10 nm). Switching fields is a strong function of defects in ultrathin finger electrode type systems. We also show how polarization vector configures itself in favor of the highly inhomogeneous field formed under applied bias in the finger

electrode case for a film under tensile stress. Thus, switching and the related sensing technique has to be considered accordingly in applications. Presence of a bottom electrode for the case of the finger electrode capacitor also has a substantial impact on electrical properties. The hysteresis and domain characteristics of the two capacitor geometries as a function of interface conditions and defects are discussed for $BaTiO_3$ strained on compressive and tensile single crystal substrates.

*Corresponding author e-mail: burc@sabanciuniv.edu

1. Introduction

Long term stability of a switchable ferroelectric polarization (*P)* in epitaxial thin films have been a topic of interest for many research groups as well as the integrated circuit (IC) industry. The designs employing a ferroelectric polarization in a capacitor-type structure have mostly focused on systems with the ferroelectric being sandwiched between two electrodes through which the data or agent signal can both be generated and sensed in a particular application. With the down-scaling of ICs to dimensions not larger than a few tens of nanometers, size reductions in the thickness and lateral sizes of capacitors have become a strict requirement. It is now well known experimentally, followed by theoretical explanations, that ferroelectrics, when in thin film form sandwiched between two metallic electrodes, can suffer from the formation of an utterly non-ferroelectric layer at the film-electrode interface [1-11]. Thus, if the bound charges due to abrupt termination of *P* at the interfaces are not fully screened, electrical domains form in a way so as to minimize the so-called depolarizing field in the film interior [3]. Very recently, the polarity of the interfaces have become to the attention of Wang *et al.* as a possible effective mechanism determining the limit to ferroelectric behavior [12]. Moreover, migration of ionic species under fields emanating from inhomogeneities, especially oxygen vacancies, towards domain-domain and metal-film interfaces contribute to the situation [13-15]. Such processes have been a limiting factor in utilizing ferroelectric thin films in a range of applications, not mentioning fatigue problems that have been partly attributed to the aforementioned phenomena [3].

While the sandwich type capacitor (SC) is the most famous the geometry studied, the interdigitated finger electrode type capacitors (IFEC) have attracted some limited attention of a few groups [16-20]. IFECs have mostly been on the agenda for tunable device applications. From a memory point of view, at a first glance, what appears to be promising for such finger electrode ferroelectric capacitor systems is that an in-plane P might not suffer from any depolarizing effects originating from the condition that $\nabla \bullet D = 0$ at an interface if the film material is a good insulator. The latter is of course true if an in-plane P is possible to stabilize via a tensile misfit, for instance. Therefore, a switchable P that is minimally impacted by the film-electrode interface conditions might be feasible to tailor. Furthermore, in case of diffusion of ionic species and vacancies under cyclic applied fields, the potential drops driving such formations occur at larger distances, meaning that a longer-lasting benefit from the ferroelectric P might be realized. In addition, due to boundary condition dependence of defect fields, a relatively weaker coupling of in-plane P to these fields might be expected. A possible disadvantage, however, is that the geometry of the finger electrode capacitor could be a limiting parameter in design of ICs employing functional components. In spite of the geometrical limitations, the effect of the electrostatic boundary conditions on the P stability and the Curie point in interdigitated finger electrodes remains as a topic studied in a very limited number of works.

In this article, we study the phase transition characteristics and electrical properties of [001] $BaTiO_3$ (BT) grown epitaxially compressive (CSC) and tensile (TSC) perovskite type [001] single crystal substrates to exemplify the effect of electrostatic boundary conditions on the physical properties. We carry out our work for sandwich type

thin film capacitor geometry in the BT/CSC system and for interdigitated finger electrodes in the BT/TSC. CSC substrates usually favors an out-of-plane *P* in the BT due to the in-plane compressive misfit strains while TSC induces an in-plane *P* owing to the large tensile misfit with BT. Employing the Landau-Ginzburg-Devonshire (LGD) functional in a two dimensional frame, we compare and contrast on the differences of properties for the two capacitor geometries with dead layers at the film-electrode interfaces and reveal the dramatic differences in the 'defect sensitivities' of the two geometries. The electrostatics of the systems are defined through the Maxwell equations, potential at the film-electrode and film-vacuum interfaces and the thickness as well as the polarizability of the dead layers in all geometries. To check the inertness of the ultrathin film capacitors against charged defects, we also analyzed the two geometries in the presence of frozen in *P* sites that represent non-ferroelectric dipoles due to an ionic vacancy. We find that such frozen in defect complexes due to ionic vacancies can alter the electrical domain configurations and hystereses in SC films but not so profoundly in IFEC films.

2. Theory and Methodology

In this section we give the governing equations and boundary conditions used to obtain field and temperature dependent characteristics of the ferroelectric thin film capacitors. A two dimensional grid is constructed that has 400*n* x *kn* cells where *k* (400) is the number of cells along the film thickness (width) and each cell, *n*, has a dimension of 0.4 nm, nearly the lattice parameters of well known pseudocubic perovskites such as

BT to imitate the order of lengths at which P can vary in the system compared to real systems. Polarization is obtained by solving the equations of state derived from the LGD free energy for all P in our system for an epitaxial monodomain (001) ferroelectric film on a (001) cubic substrate coupled with the Maxwell equation for dielectric displacement employing a finite difference discretization. The strain states of the films determine the stable P components. We first present the general approach in the following paragraphs and whether a SC type or a IFEC type is considered will depend on the way in which potential is specified at the system boundaries. The latter will be described in the forthcoming paragraphs. The total volumetric free energy of the ferroelectric thin film capacitor system is:

$$F_T = \int_V \left[w(F_0 + F_P + F_E + F_G - F_{ES}) + (1-w)F_{DL} \right] dV \qquad (1)$$

where w is a step-wise function defining the interface between the dead layer and the ferroelectric as:

$$w=1 \text{ when } -h/2 \le z \le +h/2$$

$$w=0 \text{ when } -h/2-s < z < -h/2 \text{ and } +h/2 < z < s+h/2, \qquad (2)$$

and s is the dead layer thickness (one unit cell in this work when present), h is the thickness of the ferroelectric layer. The electrode-dead layer interfaces are at $-h/2-s$ and $s+h/2$ respectively. Note that $s = 0$ indicates the absence of a dead layer, i. e., a perfect film-electrode contact interface. F_0 is the energy of the paraelectric state and is taken as zero due to the absence of order-parameter related terms. F_P is the energy due to the presence of P and is given by

$$F_P = \alpha_1(P_1^2 + P_2^2 + P_3^2) + \alpha_{11}(P_1^4 + P_2^4 + P_3^4) + \alpha_{12}(P_1^2P_2^2 + P_1^2P_3^2 + P_2^2P_3^2) + \alpha_{111}(P_1^6 + P_2^6 + P_3^6) + \alpha_{112}[P_1^4(P_2^2 + P_3^2) + P_2^4(P_1^2 + P_3^2) + P_z^4(P_1^2 + P_2^2)] + \alpha_{123}P_1^2P_2^2P_3^2 \quad (3)$$

where P_i (i=1,2,3) are the components of P in the ferroelectric state, and α_i, α_{ij}, and α_{ijk} are the dielectric stiffness coefficients (Compiled from Ref. 21). F_E in Eq. (1) is the internal elastic energy both due to the misfit between the film and the substrate as well as the self-strain in the ferroelectric state given by:

$$F_E = \frac{1}{2}C_{ijkl}\left(\varepsilon_{ij} - \varepsilon_{ij}^0\right)\left(\varepsilon_{kl} - \varepsilon_{kl}^0\right) \quad (4)$$

where the C_{ijkl} are the elastic stiffnesses for a cubic crystal, $\varepsilon_{11} = \varepsilon_{22}$ and is the film-substrate misfit strain in the pseudocubic limit along x and y, ε_{ij}^0 is the transformation strain due to the paraelectric-ferroelectric phase transition in the film and is given by:

$$\varepsilon_{ij}^0 = Q_{ijk}P_k \quad (5)$$

with Q_{ijk} being the electrostrictive coefficient tensor for a cubic crystal. The shear components of stress in (4) are taken as zero due to the traction-free film surface. The in-plane biaxial misfit state with equal orthogonal components due to epitaxy require that $P_1 = P_2$, and the rest of the equations are given hereafter accordingly. We assume two values of misfit in the simulations (compressive and tensile) for BT in order to analyze the stability of P under given electrostatic boundary conditions in sandwich and finger electrode geometries. The gradient energy in Eq. (1) we employ is:

$$F_G = G_{33}\left(\frac{dP_3}{dz}\right)^2 + G_{31}\left(\frac{dP_3}{dx}\right)^2 + G_{13}\left(\frac{dP_1}{dz}\right)^2$$
$$+ G_{11}\left(\frac{dP_1}{dx}\right)^2 + G_{23}\left(\frac{dP_2}{dz}\right)^2 + G_{21}\left(\frac{dP_2}{dx}\right)^2 \quad (6)$$

where G_{ij} are the gradient energy coefficients. For the sake of convenience, we shall assume that the gradient energy coefficient is isotropic, and thus $G_{33} = G_{31} = G_{13} = G_{11} = G_{23} = G_{21} = G$. G= $5\text{x}10^{-11}$ and is proportional to $\delta^2 (T_C / 2\varepsilon_0 C)$ with δ being the correlation length (at the order of a unit-cell far below the transition point), T_C the Curie point, ε_0 the permittivity of free space and *C* the Curie constant. We also neglect the gradients in P_2 along *y* within the two dimensional limit. F_{ES} is the electrostatic energy of the system that arises due to the electrostatic boundary conditions of the capacitors as well as gradients of *P* and is:

$$F_{ES} = -(E_x P_1 + E_z P_3) \quad (7)$$

for $w = 1$ where E_x and E_z are the in-plane and out-of-plane components of the electric field respectively. F_{DL} is simply the energy of the dead layer that is assumed to be a linear dielectric and is given by (for $w = 0$):

$$F_{DL} = \varepsilon_0 \varepsilon_r (E_x^2 + E_z^2) \quad (8)$$

The field components in (7) and (8) are computed from the Maxwell relations as prescribed in the forthcoming paragraphs, ε_r is the dielectric constant of the dead layer and is assumed to be isotropic for convenience. Minimization of Eqn. (1) for *w*=1 yields the Euler-Lagrange relations as:

$$\frac{dF_T}{dP_3} - \frac{d}{dz}\left(\frac{dF_T}{df_1}\right) - \frac{d}{dx}\left(\frac{dF_T}{df_2}\right) = 0,$$

$$\frac{dF_T}{dP_1} - \frac{d}{dz}\left(\frac{dF_T}{df_3}\right) - \frac{d}{dx}\left(\frac{dF_T}{df_4}\right) = 0 \qquad (9)$$

with $f_1 = dP_3/dz$, $f_2 = dP_3/dx$, $f_3 = dP_1/dz$ and $f_4 = dP_1/dx$. From Eqns.(9) and (1), the equations of state for the ferroelectric layer are written as:

$$G\left(\frac{d^2P_3}{dz^2} + \frac{d^2P_3}{dx^2}\right) = 2\alpha_3^m P_3 + 4\alpha_{13}^m P_3 P_1^2 + 4\alpha_{33}^m P_3^3 + 6\alpha_{111} P_3^5 + \alpha_{112}(4P_3P_1^4 + 8P_3^3P_1^2) + 2\alpha_{123} P_3 P_1^4 - E_Z \qquad (10a)$$

$$G\left(\frac{d^2P_1}{dz^2} + \frac{d^2P_1}{dx^2}\right) = 2\alpha_1^m P_1 + 2(2\alpha_{11}^m + \alpha_{12}^m)P_1^3 + 2\alpha_{13}^m P_1 P_3^2 + 6\alpha_{111} P_1^5 + 2\alpha_{112}[3P_1^5 + 3P_1^3P_3^2 + P_1P_3^4] + 2\alpha_{123} P_1^3 P_3^2 - E_X \qquad (10b)$$

in the ferroelectric film $(w = 1)$ where the α_3^m, α_{13}^m, α_{33}^m are the renormalized dielectric stiffness coefficients, modified by the misfit strain, the electrostatic field, and the two-dimensional clamping of the film [33]. The dead layer, when present, is assumed to be a high-*k* dielectric whose dielectric constant, ε_r, is 20 to exemplify its effects. The electric fields in both the ferroelectric layer and the dead layer are computed from the gradient of the electrostatic potential ϕ,

$$E_Z = -\frac{d\phi}{dz},\ E_x = -\frac{d\phi}{dx} \qquad (11)$$

The electrostatic potential is found at each point in the system as function of *P* components using the Maxwell relation in the absence of free charges,

$$\nabla \cdot D = 0 \qquad (12)$$

where $D_Z = \varepsilon_b \varepsilon_0 E_Z + P_3$ and $D_X = \varepsilon_b \varepsilon_0 E_X + P_1$ in our two dimensional case with ε_b being the background dielectric constant (taken as 10 in this work) and the fields can be inserted into (12) with their forms given in (11). Equations (11) and (12) relate the strength of the depolarizing electric field to the variations in the components of *P* both in the film as well as the ferroelectric-dead layer interface. The boundary conditions we employed for $P_{1,3}$ are

$$\left[P_1 + \lambda \frac{dP_1}{dz} \right]_{z=-\frac{h}{2}-s,\frac{h}{2}+s} = 0 , \left[P_3 + \lambda \frac{dP_3}{dz} \right]_{z=-\frac{h}{2}-s,\frac{h}{2}+s} = 0 \qquad (13)$$

at the top and bottom electrode-film interface of the ferroelectric where the extrapolation length, λ, is taken as infinite. Periodic boundary conditions are used along the sides (*x*-axis), i. e.,

$$P_3(z, x = 0) = P_3(z, x = L) , \; P_1(z, x = 0) = P_1(z, x = L) \qquad (14)$$

We apply Dirichlet boundary conditions to solve *P* in both the sandwich type and finger type electroded systems. At the dead layer-electrode interfaces of the SC, *-h/2-s* and *s+h/2*, $\phi = 0$ at top and bottom interfaces correspond to total charge compensation while periodic boundaries are adopted along *x* as given in (13). Figure 1a shows the SC geometry. In the case of the IFEC, ϕ is given for the two electrodes as shown in Figure 1b. The free surfaces in the IFEC capacitor has to satisfy Eqn. (12) and periodic boundaries are employed along *x*. It is important to remind here that, in both the SC and IFEC, the charge compensation is at the dead layer-electrode interfaces, meaning that bound charges are partially screened at the ferroelectric-dead layer interfaces depending on the dead layer thickness. Of course, one must note that the IFEC case has only induced P_3 along *z* upon application of a bias to the finger electrodes. In order to demonstrate the

effect of a bottom electrode in the IFEC system, we also assigned $\phi = 0$ when specified as this would make a serious impact on the field distribution in the IFEC. Moreover, the electrode thickness in the IFEC is chosen finite, proportionate with the film thickness (10 nm thick) and the electrostatic solution for the IFEC also contains the fields in vacuum.

Equations (10) – (12) are solved simultaneously employing a Gauss-Seidel iterative scheme subject to boundary conditions mentioned above and (13) and (14) for *P*. The simulations always start with small fluctuations of *z* and *x* components of *P* components around zero that later on develop into the domain structure depending on dead layer and fılm thickness. We limit ourselves to 5000 iterations converging to a difference of 10^{-8} between consecutive iterative *P* solution steps when ferroelectricity exists. The defects, when present, are assumed to be frozen-in *P* complexes in the lattice where we basically assign a fixed *P* to randomly chosen sites, with the restriction that they cannot be too close to each other in order to test long-range effects. Their positions are fixed with respect to the bottom electrode/free surface coordinates. Thus, their positions along *z*-axis with respect to z=0, the midsection of the film along *x*, is automatically altered when film thickness changes. This mostly impacts the symmetry of the defect positions with respect to the midsection of the film for ultrathin films but is still good enough to demonstrate their effects in ultrathin structures. We also must add here that, within the 2D limit of the study, our results might not be exactly representing the behavior of 3D systems with very few defects due to variation in the averaging of properties. On the other hand, they can be compared to 3D systems with relatively high density of defects where averaging over the volume will be close to the averaging over a 2D slice of the system.

To get the electric field dependent behavior of the films in the SC geometry, we simply change ϕ on the bottom electrode and assing the other $-\phi$ and thus the film sees an electric field. For the IFEC films, we do so for the finger electrodes grown on the top surface of the film. A triangular signal for ϕ is used to get the hystereses of the films with maximum voltage drop amplitudes chosen depending on the film thickness for the SC and inter-electrode distance for the IFEC. The IFEC films see the electric field between the finger electrodes where each electrode attains the negative value of the other. In the latter, the electrode thicknesses are 8 nm and due to the free surfaces exposed between the electrodes, we solve the ϕ outside the IFEC films, too, to get the correct picture for its distribution. These IFEC films also experience fields between the finger electrodes and a grounded bottom electrode when there is one. The signal consists of 100 steps between -2V and +2V. At every incremental bias step, we allow the films to reach their near-equilibrium *P* configuration. Hence, the hystereses in our simulations are in the quasi static limit for both the SC and the IFEC geometry.

We considered in this study the heteroepitaxial (001) BT films fully strained on a non-ferroelectric

1. (001) hyphothetical cubic perovskite substrate inducing a -1% misfit with pseudomorphic top and bottom metallic electrodes (SC) and,

2. (001) hyphothetical cubic perovskite substrate inducing a 1% tensile misfit with pseudomorphic interdigitated metallic finger electrodes (IFEC).

We assumed the above hypothetical substrates as working with real substrates introduce the strain due to the different thermal expansion coefficients into the phase transition characteristics. This makes it difficult to directly compare the impact of the

electrostatic considerations for both the SC and IFEC. Moreover, choosing a real compressive and a real tensile substrate that induce directionally identical $|\varepsilon_{11} = \varepsilon_{22}|$ is nearly impossible that would complicate the comparisons pursued in this work. One must also note that the in-plane strains couple to P components via Q_{11} and Q_{12} for films with P along z and x axes respectively. Because Q_{11} and Q_{12} are different, the Curie points should be expected to differ even when $|\varepsilon_m^C| = |\varepsilon_m^T|$ where ε_m^C and ε_m^T are the misfits of the films under compression (SC film) and tension (IFEC film). However, the approach presented here can easily be adapted to any pseudocubic ferroelectric perovskite film on real substrates. The values of the dielectric stiffness coefficients and other thermodynamic parameters of BT entering the calculations are taken from Ref. 21. Simulation results are presented for films of 8 nm, 16 nm thickness in SC and IFEC geometries.

3. Results and Discussion

In the forthcoming paragraphs and subsections we discuss the results for the ferroelectric SC and IFEC films at RT, under a fıxed applied bias as well as a triangular signal. In each subsection, we analyze the effect of dipolar defects whose schematic is given in Figure 2: A frozen-in, dipole couple or so-called *p*-type complex formed due to a missing O vacancy where the B-site ions are shifted into opposite corners in the two neighboring unitcells to reduce repulsive forces under fully ionic consideration whose schematic is given in Figure 2. This is a so-called *p*-type defect [20] and is similar to the

defect type whose mechanism of formation was reported in Ref. 21 accompanied by relaxation of the atomic forces

Due to the different variations in electrostatic potential around the types of defects menitoned above, they are expected to have a quite complicated impact on the properties in both the SC and the IFEC films. We assign the components in such a way that a fixed *P* at a site can have *x* and *z* components with either a negative or a positive sign along each axis. At the atomic level, such frozen-in dipole sites are the result of ionic vacancies where a local electrostatic imbalance is overcome via a displacement of anions or cations depending on the type of vacancy. Atomistic first principles studies have reported substantially high dipole moments for vacancy-induced dipoles, comparable to or more than the moments of spontaneous ferroelectric dipoles [22]. Keeping in mind the results of these studies, we work with frozen-in, non switching defect-dipole sites whose values are assigned as 0.25 C.m/m^3, close to the bulk $BaTiO_3$ *P* at RT. We discuss our results particularly in the light of these considerations in the SC and IFEC geometries.

3.1. Ferroelectricity at Room Temperature in SC Thin Film Capacitors

3.1.1. Existing dead layer (s=1)

We first focus on the way *P* configures itself at RT under the 1 % compressive strain and electrostatic conditions imposed in the SC geometry. While the general characteristics of the ferroelectric SCs, particularly in the presence of dead layers, are well established for equilibrium states, we give our results for a full comparison with the ferroelectric IFEC films. The RT P_z domain structure for the defect-free SC film is given

Figure 3a for two different thicknesses: 8 nm and 16 nm thick films. The dead layer thickness, when present, is fixed in both cases to one unit cell thickness (s=1). The 8 nm thick film is stable in the paraelectric phase (not shown) while the 16 nm film is in a ferroelectric multidomain state with a domain period of 22.8571 nm, given in Figure 3a. (One period here consists of a + and – polarized cluster). Both films are in a single domain ferroelectric state in the absence of dead layers with exactly the same P values and is not given here for brevity. Please note that the minimum dead layer thickness we work with in this study is 0.4 nm and is equal to the discrete cell size with $\varepsilon_r = 20$. Smaller lengths at which the electric field permeates into the electrodes or different values of ε_r would impact the domain stabilities in films around or less than 8 nm thickness but is outside the scope of this article.

We would like to discuss now the case of 16 nm thick film with s=1 in the presence of the type of defects described at the beginning of this section. The domain structure is given in Figure 3b-c. The defects are regularly spaced along x but with slightly different positions along z. We try to keep a distance that is much larger than the strong spatial influence lengths of these defects to examine the collective long-range effects. In the presence of the P-TYPE type defect (See the first paragraph of Section 3), one immeadiate observation one can make is the increase in the domain period and its deviation from uniformity. Such a deviation from uniformity is due to the fact that domains are trying to line up in a compatible fashion with the defect-imposed configuration. Still, presence of domains implies that the depolarizing field is the dominant term in determining the stable state of the system.

3.1.2. No dead layer (s=0)

Choosing s=0, i. e. no dead layer, we run our simulations for the 8 nm and 16 nm films again for the p-type type defects whose results are given in Figure 4a-c. The 8 nm film is in a single domain state when the electrode potentials are zero, corresponding to full charge compensation at the interfaces. Introducing the p-type defects changes the spatial solutions of P_z around the defect sites and leads to a reduction in P_z along z in their vicinity in a film with $-P_z$. There are also very small regions, consisting of a few discrete-cells, right near the defects where the defect field actually passivizes the remanent P_z. The butterfly-like shapes of regions where P_z is altered is mostly due to the electrostatic potential of the p-type defect and in part due to the minimization of the gradient energy.

The above conclusions withdrawn for the 8 nm film does not differ much for the case of the 16 nm film. p-type defects do not trigger formation of domains with opposite orientation and only modify the P_z in the vicinity with small, ferroelectrically dead cells in the neighborhood of the defect sites. There is no domain formation but just regions where P_z is slightly suppressed or pinned in the vicinity of the defects. The potential drops starting from the defect sites slowly decay towards the electrodes and are mostly confined to distances of about not more than 10 nm near the largest gradients in P_z. However, defects in higher densities with dipole moments possibly higher than the remanent P might have effects extending to larger distances than that of mentioned here.

3.2. Ferroelectricity at Room Temperature in IFEC Thin Film Capacitors

Using exactly the same method described in Section 2, but with the appropriate BCs, we provide our RT results for the IFEC films in this section. During the simulations of the domain states in the IFEC films, we note that the presence or absence of a dead layer (s=0 or s=1 respectively) has no significant impact on the domain morphologies of the 8 nm and 16 nm thick IFEC films with or without defects. Therefore we give in this section our results for s=1 to avoid repetition of similar plots and evaluation. Moreover, in order to reveal the volume of the IFEC films that switch via response to applied bias, we emphasize here the states under bias that is sufficient to saturate the P_x in the plane of the film followed by removal of the bias. The latter is to display the domain configuration under remanence. The electrode geometry is already given in Figure 1 and we consider IFEC films only with top finger electrodes throughout the discussion. For the RT results herein presented, the presence of a bottom electrode also has no apparent influence on the *P* configuration near saturation bias followed by zero bias. Due to this reason, the results shown here are in the absence of a bottom electrode. The effect of a bottom electrode, however, becomes very important in switching characteristics, particularly the coercive fields of the IFEC films and related details are discussed in Section 3.4. We also would like to remind here that the bias fields for which the domain states are given in this section are higher than the coercive values for the 8 and 16 nm thick IFEC films.

Solution of the P_x and P_z starting from fluctuations around zero under 1% tensile misfit at zero bias develop into a single domain state of remanent P_x pointing in either $-x$ or $+x$ direction with zero P_z and these are not given here for brevity. Applying 1.5V and -

1.5V bias on the electrodes respectively, we show in Figure 5a-c the in-plane domain state stability of P_x in the 8 and 16 nm thick defect-free films. The resultant configuration is the consequence of the inhomogeneous distribution of the field inside the film where the field changes sign in different portions of the film. Removal of the bias leads to an apparently stable remanence of P_x that changes sign along x both in the 8 nm and 16 nm thick films as displayed in Figure 5b-d. Due to the condition of the remanent P being parallel to the interface, there is no jump in dielectric displacement at neither z=h/2 or z=-h/2, hence no depolarizing fields along x when external bias is zero. Therefore the 8 nm and 16 nm IFEC films do not suffer from thickness effects compared to the SC ones. P_z has zero solution at zero bias due to the tensile misfit but attains spatially varying non-zero solutions under bias due to the obvious reason: Potential drops from the finger electrodes towards bottom of the film. Note that s=1 on each surface. In the next paragraphs, we discuss the results for the 8 nm and 16 nm thick IFEC films seperately.

When the aforementioned type of defects are present with s=1, the above picture for the 8 nm film only slightly changes. Turning our attention to Figure 6a-b for the 8 nm IFEC films with *p*-type defects, we see no induction of any type of nano-sized domains. P_x is still mostly in favor of the local field direction under the bias on the finger electrodes alike the defect-free case. This is because the remanent P_x is lying in the plane and that there is no specific boundary potential specified along x, unlike the boundaries along z. Referring to Figure 6b, upon removal of the bias, the P_x configuration does not change much and more or less sustains its state in the biased case for *p*-type defects. The interface between the P_x components pointing along $-x$ and $+x$ directions undergoes a slight or even negligible rearrangement. P_z, after removal of the bias, is zero except

components forming due to slight rotations of P near the interfaces where P_x changes sign. Therefore, we observe from Figure 6 that, even in the presence of dipolar defects, there is hardly any loss of the spatial state in between the electrodes attained under bias. The common observation in the simulations of the IFEC films here is that defects act as local perturbation centers to the order state and do not trigger domain formation. However, these RT results obviously do not imply that the hystereses and phase transition characteristics for the defected and defect-free 8 nm thick IFEC films will also be similar.

Looking at the response of the 16 nm IFEC film with *p*-type defects given in Figure 7, we again see that the configuration of P_x under bias (Figure 7a) and zero bias (Figure 7b) are similar, again with the exception of the interface asymmetry with respect to the midpoint of the structure in the 16 nm IFEC with *p*-type defects. The same configurational trend of P_x distribution as in the 8 nm IFEC film is observed but a larger switched volume is present in 16 nm film. Stability of P_x under applied bias and upon removal of the bias in the IFEC films with defects is only slightly altered. If examined carefully via Figure 6 and Figure 7, the defects near the bottom interface of the 16 nm film are more visible under zero bias and appear to have a larger area of influence in contrast to the 8 nm thick one. This is because of the decay of the magnitude of the electric field into the film volume away from the finger electrodes and that the "defect configured P_x" becomes more prominent compared to applied field effects. Regions in the vicinity of the electrodes are naturally under a stronger influence of the applied bias and this overrides the induction effects due to dipolar defects as in the 8 nm thick film. But again it should be borne in mind that the stabilities of the P_x components shown in the colormap plots do not reveal how the hystereses would be impacted by these defects.

Overall, the P_x component in the IFEC films under tensile in-plane misfit strains appear to be stable without any electrical domain complications similar to that of observed in the SC films. The remanence mentioned for the IFEC geometry, on the other hand, is the stability of a switchable but a local P_x with respect to the electrode positions and widths. The electrostatics fields of the *p*-type defects is also more complicated as there is an abrupt sign change of P_x and P_z at the sites neighboring missing ion. But we did not observe any dramatic variations in the results in IFEC films with *p*-type defects. Sharp, square hystereses are obtained via tracking the P_x in the mid-section of the IFEC films which are to be discussed in the next section.

3.3. Characteristics of the Hysteresis Loops in SC Films

In order to keep as reference, we first give the hysteresis loops of the defect-free 8 nm and 16 nm thick films with and without dead layers in the quasi-static limit in Figure 8. The vertical and horizontal axes of the hystereses consist of $<P_z>$ and applied bias respectively. We note that the films without dead layers have nearly rectangular hystereses while this scenario is dramatically different when s=1 for both thicknesses. The 8 nm film has only a linear variation of P_z with field, nearly overlapping with the defected case (not given in the Figure) and the 16 nm film has a double-loop hysteresis. The former is because the 8 nm film is in paraelectric state and the latter result is due to the stabilization of domains at low-to-mid bias values. Similar results were also obtained by Ahluwalia and Srolovitz [25] but for much thicker dead layers with very high (at the order of 200) dielectric constant.

Rather than mentioning the effects of defects for the 8 nm SC film in a seperate section, we discuss their effect in this paragraph as they do not alter the hystereses significantly. The presence of defects, only introduces small distortions to the hystereses. Spatially we note that there is a small volume around the defects that has a non-zero, finite P_z along both z and x. This is expected as the abrupt decay of the P_z and P_x away from the defect sites create electrostatic fields in the vicinity through Eqns. (11) and (12) , polarizing the medium around them.

Figure 8b shows the simulation of the quasi-static hysteresis of the 16 nm film with *p*-type defects. Defects deform the hysteresis in a non-uniform manner, which is otherwise a clear, symmetrical double-loop. The loop in the negative bias region is slightly displaced towards higher bias in the negative direction due to the asymmetry of the defect position in the films. Besides the non-uniformity of the hystereses in the films with defects, an important observation is that the films with defects could exhibit higher dielectric constants at low-to-mid bias values. We claim so due to the fact the applied bias-<*P*> curve in this region is steeper than for the defect free film. Overall, depolarizing fields due to the presence of a non-ferroelectric layer at the film-electrode interfaces strongly dominate over defect related effects in SC films.

3.4. Characteristics of the Hysteresis Loops in IFEC Films

3.4.1. No defects

Applying the the triangular bias signal to the top electrodes where each attains the opposite sign of the neighboring electrode, we extracted the hysteresis loops of the IFEC films with in-plane P (P_x). It is clear that the field distribution in this geometry is not uniform along the film volume and that parts of the films switch in opposite directions. The region shown with the arrows between the electrodes are tracked to probe the P_x and P_z as a function of applied bias signal. Again, due to the inhomogeneity of the field distribution, we probed P_x and P_z in the middle section of the aforementioned region for better clarity. Noting that the presence or absence of a dead layer does not make a difference in the IFEC geometry, we studied this system in the presence of a dead layer with s=1. The very reason for this is that there is no remanent P component in the dielectric displacement normal to the electrode-film interface and that the Px is not impacted by the condition $\nabla \bullet D = 0$, the main source of the depolarizing field in the ferroelectric. In addition, we also computed the average dielectric displacement at the surface exposed between the top finger electrodes to identify whether a signal here is possible to tailor during switching of P_x.

Figure 9 displays the hysteresis loop for the applied bias-P_x in the 8 nm and 16 nm thick IFEC films for s=1 and no bottom electrode where P_x in the middle of the region between the electrodes was tracked. We do not give the results for s=0 as there appears to be no significant change in the response of P_x compared to s=1 case. This way, we avoid evaluation of identical plots and data and focus only on results that clarify the governing phenomena impacting the hystereses behavior. In the absence of defects, there is a nearly square hysteresis in both IFEC films and the behavior is quite identical. Also in Figure 9, we give the impact of the presence of a bottom electrode in the IFEC films:

Both the 8 nm and 16 nm films switch now at a lower coercive field in the thermodynamic limit. Moreover, the films without the bottom electrodes have a displaced hysteresis towards the positive bias, indicating it is more difficult for P_x to switch from $-x$ to $+x$ direction in the middle region between the electrodes. This difference in the switching behavior in the IFEC films with bottom electrodes is due to the presence of a large out-of-plane electric field formation that stabilizes a z component of P, namely P_z. For P_z, right near the coercive bias of P_x we find relatively large values for its solution and nearly zero elsewhere in the planar bias range of interest. Therefore the film passes through an "induced" monoclinic state during switching favored by the field along z axis which seems to reduce the coercive field value for P_x. Moreover, the hysteresis of the IFEC films with no bottom electrode is significantly displaced along the bias axis: A clear implication of the difference in the potentials at the top and bottom surfaces.

The thickness dependent effects in IFEC films with dead layers do not have an as profound an effect on remanent P stability as in SC films. Moreover, this "nearly dead-layer independence of polarization" of IFEC films is a very important and advantageous aspect that could be tailored in device design. We also would like to remind here that the hystereses of the IFEC films were obtained via tracking the P_x states of the region in the middle of the two electrodes. The average P_x of the entire film does not yield a net hystereses due to the inhomogeneous nature of the field distribution in the given electrode positions and is not given here for brevity. On the other hand, we find that D_z, on the exposed surface between the top-electrodes, especially in the presence of a bottom electrode, undergoes abrupt variations around the coercive bias values of P_x. These peak-like abrupt variations in D_z could be useful as a sensing signal of the switching occuring

in P_x, for instance, via tracking the change of dielectric displacement along z near the bottom electrode or an electrode placed in between the top ones. One important aspect is that the sign of these peaks are thickness dependent and, in the absence of the bottom electrode, such peaks nearly disappear and become very weak or negligible. It is clear that this behavior can be attributed to the boundary condition at the bottom interface. This is because of the depolarizing fields taking effect that oppose P_z during the switching of the P_x and thus no clear peak-like P_z variations are observed. As such, the sign of the D_z peaks are impacted by this. The ease with which P_z switches also impacts the switching characteristics of P_x as demonstrated.

3.4.2. Defects Present

We now discuss the effect of *p*-type type defects on the 8 nm and 16 nm thick IFEC films for s=1. In this section, we again skip the discussion of the characteristics of the hystereses for s=0 because as we implied earlier that whether s=0 or s=1 has only a negligible effect on the behavior of P_x in the IFEC films. For this reason we keep our focus on the defected IFEC films with s=1 for a more compact and well-organized discussion. As already explained previously, the behavior of P_x is more complicated in the overall film volume compared to that of the SC films. Owing to the highly inhomogeneous fields during hystereses extraction tracking the P_x in the middle section of the film, between the electrodes, is what we again pursue in order to justify defect related effects. One important phenomena is that, when defects are present, the P_x in the central region between the electrodes is influenced by their existence, even if several tens

of nanometers away from defect sites. This is a clear implication of the long-range effects of frozen-in dipole complexes formed due to ionic vacancies. We next discuss the alterations in the hysteresis loops in the 8 nm and 16 nm films with defects.

The presence of *p*-type defects have a substantial influence on the hystereses of both the 8 nm and 16 nm thick films as seen in Figure 10. In the presence of bottom electrodes, there is a visible shift of the hysteresis loops with a slight increase in the coercive bias values. While the *P*-*V* loops in the 16 nm IFEC film are displaced along the bias axis mostly with *p*-type defects (Figure 10b), a swelling of these loops accompanies the shifts in the 8 nm film regardless of the presence of bottom electrode (Figure 10a). The increase in coercive bias is quite pronounced in the 8 nm film, indicating difficult switching. One must remember that the P_x component in the middle of the film is not under the influence of any strong depolarizing or internal bias fields originating from asymmetric boundaries. We note that due to the components of the *p*-type defect dipoles along +*x* and –x, the coercive field increases in both signs of the bias axis due to local pinning. It is very important to note that a spatially varying electric field along *z*-axis exists due to the variation of the electrostatic potential along this direction in the IFEC geometry. In addition, the fields along *z*-axis emanating from any inhomogeneity in D_z in the 8 nm IFEC film are expected to be stronger than in the 16 nm one for the obvious reason: Steeper decay of potentials in the 8 nm film compared to the 16 nm film. Just to remind, the switching bias for the perfect 8 nm and 16 nm thick IFEC structures are nearly the same when a bottom electrode is absent in both cases. Therefore we can conclude that defects in thinner IFEC structures have a stronger pinning effect. The shift of the loops have exactly the same trend in defect-free, no bottom electrode IFEC films.

Another aspect we find worth mentioning here is the slight shift of the loops in the IFEC films with defects. One would normally expect this shift to be at a minimum due to the relatively symmetric potentials created around the dipole couple. However, the position of the defects with respect to the electrodes and their assigned values already do create a highly asymmetrical distribution of the fields. Moreover, this shift will also depend on the region where the local P_x value is probed. Throughout the analysis of our simulation results, we realized that there are several factors that contribute to the way in which the hysteresis loops would shift in the IFEC films. Thus, we give here the general characteristics and trends to avoid a lengthy discussion on this aspect. It becomes particularly important to consider the defect positions with respect to the electrodes. A detailed study of the interaction between defect sites, asymmetry of the film structure and how these impact local pinning of P components will be given in a seperate study where general phase transition characteristics for IFEC films with defects will also be revealed.

Overall, despite the complicated nature of the defect effects in the highly inhomogeneous field distribution of the IFEC films, we can make some remarks to a certain extent regarding the hystereses characteristics: Figure 10a clearly reveal that the 8 nm IFEC films with defects require higher bias fields to switch P in between the electrodes. The bottom electrode strongly alters the switching characteristics of the system due to the ease with which a metastable P_z gets stabilized at coercive bias values for P_x. Switching bias and the way in which the loops shift are relatively different in the 8 nm and 16 nm thick IFEC films. The 8 nm thick IFEC system suffers more profoundly from pinning due to defects. A striking characteristic, however, to note in both the 8 nm and 16 nm IFEC films is that there is nearly no deformation of loops and they preserve

the squareness. The absence of a bottom electrode apparently eradicates easy switching in the 16 nm film with defects but no such conclusion can be arrived at for the 8 nm thick IFEC film. Despite being not so easy to miniaturize, the IFEC geometry, with efficient IC architecture, might be a feasible option to tailor owing to the nearly defect insensitive nature of the P_x remanence.

4. Conclusions

In this study, we compared the effect of electrostatic boundary conditions on RT domain structures and hystereses of ferroelectric SC type and IFEC type thin films. Due to the way in which P is stabilized under compressive and tensile misfits, tailored in SC and IFEC type capacitors, the senstivity of the systems to electrostatic BCs is dramatically different in the two types of capacitors. The SC geometry is highly susceptible to formation of electric domains once there is incomplete screening of the polarization charges at the film-electrode interface, a well established phenomena. The IFEC geometry, on the other hand, is nearly insensitive to dead layer thickness and has an alternating sign of P along the in-plane at applied bias following the direction of the in-plane fields and also after removal of bias. The IFEC swithcing is impacted by the presence or absence of a bottom electrode, implying the coupling of P_x to induced P_z near switching. Our simulations indicate that P_z makes a sharp anomaly at the coercive field of the P_x and can be used as a signal to sense switching. This signal, however, disappears when a bottom electrode is not present and switching for P_x becomes harder and quite asymmetrical.

The presence of defects in ultrathin SC and IFEC capacitors have different impacts on the hystereses: The SC loops get deformed while no such significant deformation is observed in IFEC films but a shift in the loops along the bias axis, probably accompanied by an increase in the coercive fields for thin samples. The overall effect of frozen-in dipolar *p*-type defects is that the steep gradients around the defect sites that decay towards the electrodes create strongly inhomogeneous fields. These fields, in the case of the SC type films, strongly couple to Pz while the coupling of these fields in the IFEC geometry to P_x is weaker but indirect coupling through cross terms in P_z and P_x can occur. The latter is still, however, significant enough to displace the hysteresis loops asymmetrically through the bias axis. Overall, the defects in thin IFEC films increase the coercive bias in the thermodynamic limit due to spatial pinning but no loss of remanency due to electrical domains is observed.

Acknowledgements

The authors would like to acknowledge Sabanci University for software and hardware support.

References:

1. M. Dawber, K. M. Rabe, and J. F. Scott, Rev. Mod. Phys. **77**, 1083 (2005).
2. R. R. Mehta, B. D. Silverman, and J. T. Jacobs, J. Appl. Phys. **44**, 3379 (1973).
3. A. M. Bratkovsky and A. P. Levanyuk, Phys. Rev. Lett. **84**, 3177 (2000).

4. T. M. Shaw, S. Troiler-McKinstry, P. C, Mcintyre, Ann. Rev. Mat. Sci. **30**, 263 (2000).
5. J. Junquero and P. Ghosez, Nature **422**, 506 (2003).
6. G. Gerra, A. K. Tagantsev, N. Setter, and K. Parlinski, Phys. Rev. Lett. **96**, 107603 (2006).
7. G. Gerra, A. K. Tagantsev, N. Setter, Phys. Rev. Lett. **98**, 207601 (2007).
8. Massimiliano Stengel, Nicola A. Spaldin, Nature Lett. **443**, 679 (2006).
9. Y. Yacoby, Y. Girshberg, E. A. Stern and R. Clarke, Phys. Rev. B **74**, 104113 (2006).
10. S. Prosandeev and L. Bellaiche, Phys. Rev. B **75**, 172109 (2007).
11. Zhou, C., Newns, D. M. Intrinsic dead layer effect and the performance of ferroelectric thin film capacitors. *J. Appl. Phys.* **82**, 3081 (1997).
12. Y. Wang, M. K. Niranjan, K. Janicka, J. P. Velev, M. Ye. Zhuravlev, S. S. Jaswal, and E. Y. Tsymbal, Phys. Rev. B 82, 094114 (2010). – Polar interface
13. Y. Xiao, V. B. Shenoy and K. Bhattacharya, Phys. Rev. Lett. **95**, 247603 (2005).
14. Y. Zhang, J. Li, and D. Fang, Phys. Rev. B **82**, 064103 (2010).
15. L. Hong, A. K. Soh, Q. G. Du and J. Y. Li, Phys. Rev. B **77**, 094104 (2008).
16. B. Xu, L. E. Cross and J. J. Bernstein, Thin Solid Films **377-378**, 712 (2000).
17. J. H. Haeni, P. Irvin, W. Chang, R. Uecker, P. Reiche, Y. L. Li, S. Choudhury, W. Tian, M. E. Hawley, B. Craigo, A. K. Tagantsev, X. Q. Pan, S. K. Streiffer, L. Q. Chen, S. W. Kirchoefer, J. Levy and D. G. Schlom, Nature **430**, 758 (2004).
18. K. Dayal and K. Bhattacharya, Acta Mat. 55, 1907 (2007).

19. B. Xu, R. G. Polcawich, S. Troiler-McKinstry, Y. Ye and L. E. Cross, Appl. Phys. Lett. **75**, 4180 (1999).

20. M. Y. El-Naggar, K. Dayal, D. G. Goodwin, and K. Bhattacharya, J. Appl. Phys. **100**, 114115 (2006).

21. N. A. Pertsev, A. G. Zembilgotov and A. K. Tagantsev, Phys. Rev. Lett. **80**, 1988 (1998).

22. A. P. Levanyuk and A. S. Sigov, "*Defects and Structural Phase Transitions*", Volume 6, in *Ferroelectricity and Related Phenomena*, edited by W. Taylor, Gordon and Breach Science Publishers, (1988).

23. S. Pöykkö and D. J. Chadi, Phys. Rev. Lett. **83**, 1231 (1999).

24. E. Cockayne and B. P. Burton, Phys. Rev. B **69**, 144116 (2004).

25. R. Ahluwalia and D. J. Srolovitz, Phys. Rev. B **76**, 174121 (2007).

Figure Captions:

Figure 1. (Color online) The schematic of the (a) SC type ferroelectric film and (b) IFEC type ferroelectric film examined in this work. Note that in (b) the impact of a bottom electrode is considered in obtaining the hysteresis loops and is shown with semi-transparent color here.

Figure 2. (Color online) The *p*-type defects in this study. The dashed circle in the middle denotes the missing oxygen ion while the red atoms denote the Ti ions. The arrows indicate the shift of the positively charged Ti ions, forming a antiparallel configured dipole couple of not-ferroelectric origin.

Figure 3. (Color online) P_z distribution in the 16 nm thick SC films for s=1 with (a) no defects, (b) P-TYPE type defects and (c) FID type defects.

Figure 4. (Color online) P_z distribution in the SC films for s=0 for (a) *p*-type defects in 8 nm thick film, (b) *p*-type defects in 16 nm thick film.

Figure 5. (Color online) Map of P_x in (a) 8 nm thick defect-free IFEC film under bias, (b) 8 nm thick defect-free IFEC film after bias removed, (c) 16 nm thick defect-free IFEC film under bias, (b) 16 nm thick defect-free IFEC film after bias removed.

Figure 6. (Color online) Map of P_x in (a) 8 nm thick IFEC film with *p*-type defects under bias, (b) 8 nm thick IFEC film with *p*-type defects after bias removed.

Figure 7. (Color online) Map of P_x in (a) 16 nm thick IFEC film with *p*-type defects under bias, (b) 16 nm thick IFEC film with *p*-type defects after bias removed.

Figure 8. (Color online) Hysteresis loops for (a) 8 nm thick SC film and (b) 16 nm thick SC film.

Figure 9. (Color online) Hysteresis loops and dielectric displacement along *z* (right axis) for defect-free (a) 8 nm thick IFEC film and (b) 16 nm thick IFEC film.

Figure 10. (Color online) Hysteresis loops and displacement along z (right axis) for defected (a) 8 nm thick IFEC film and (b) 16 nm thick IFEC film.

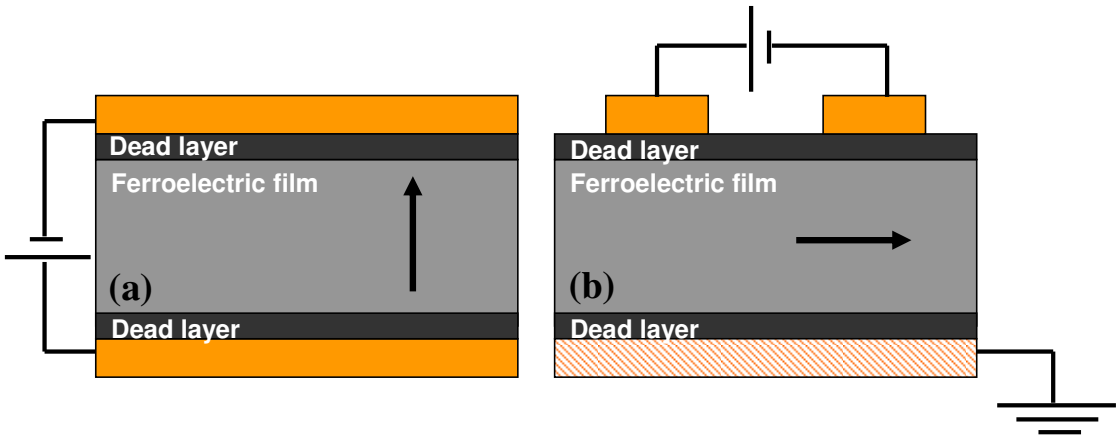

Figure 1. Misirlioglu *et al.*

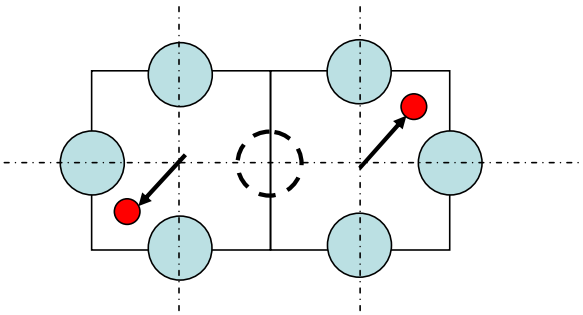

Figure 2. Misirlioglu *et al.*

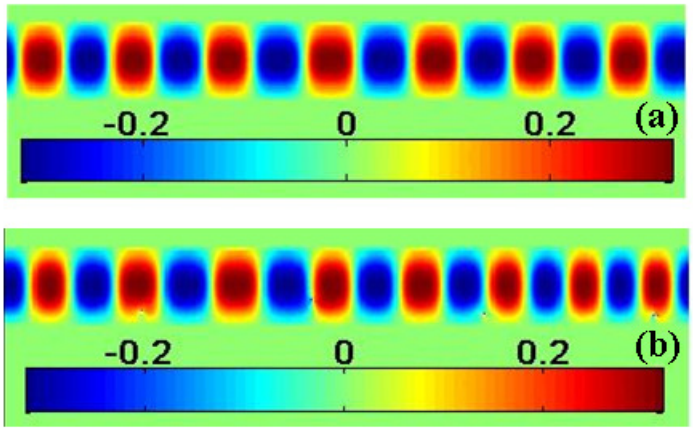

Figure 3. Misirlioglu *et al.*

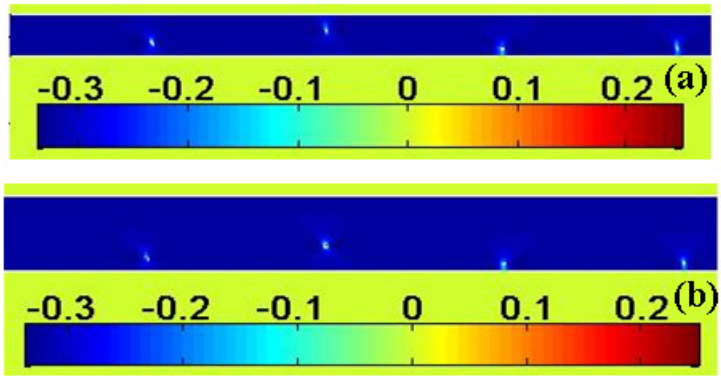

Figure 4. Misirlioglu *et al.*

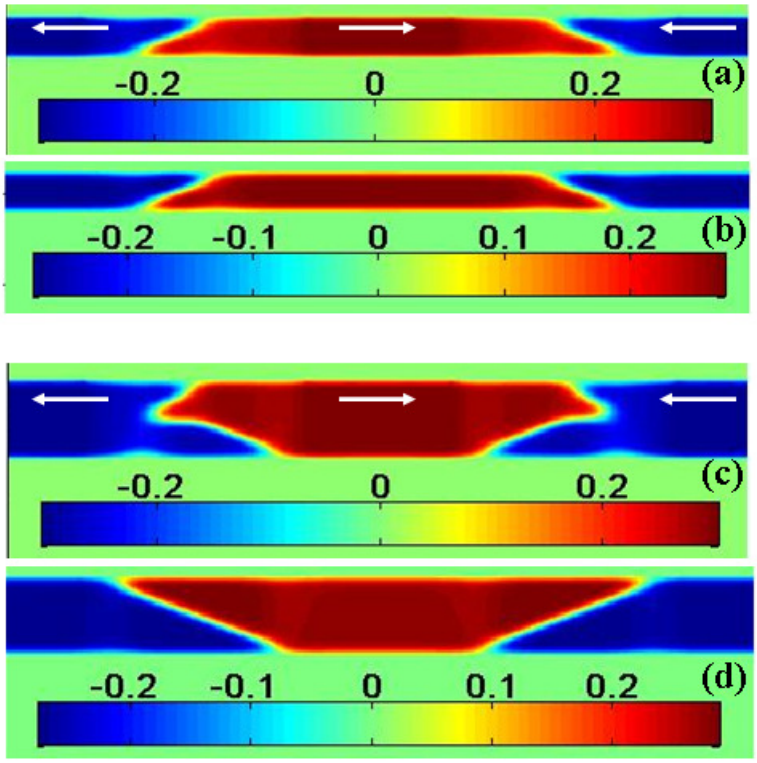

Figure 5. Misirlioglu *et al.*

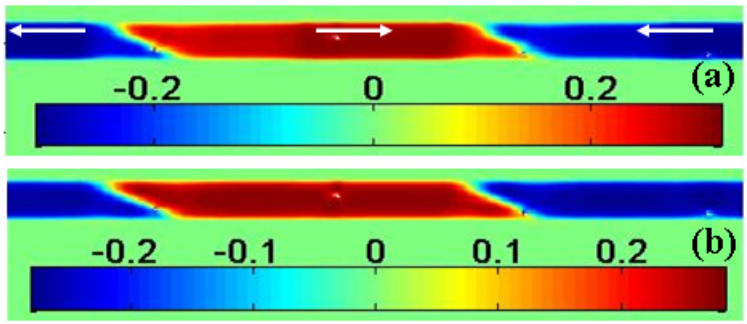

Figure 6. Misirlioglu *et al.*

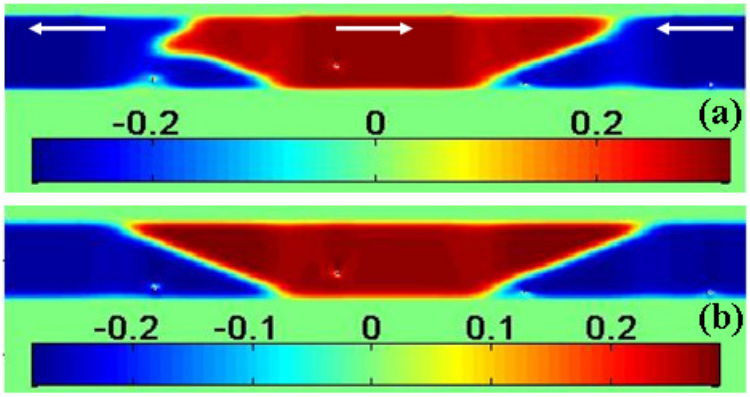

Figure 7. Misirlioglu *et al.*

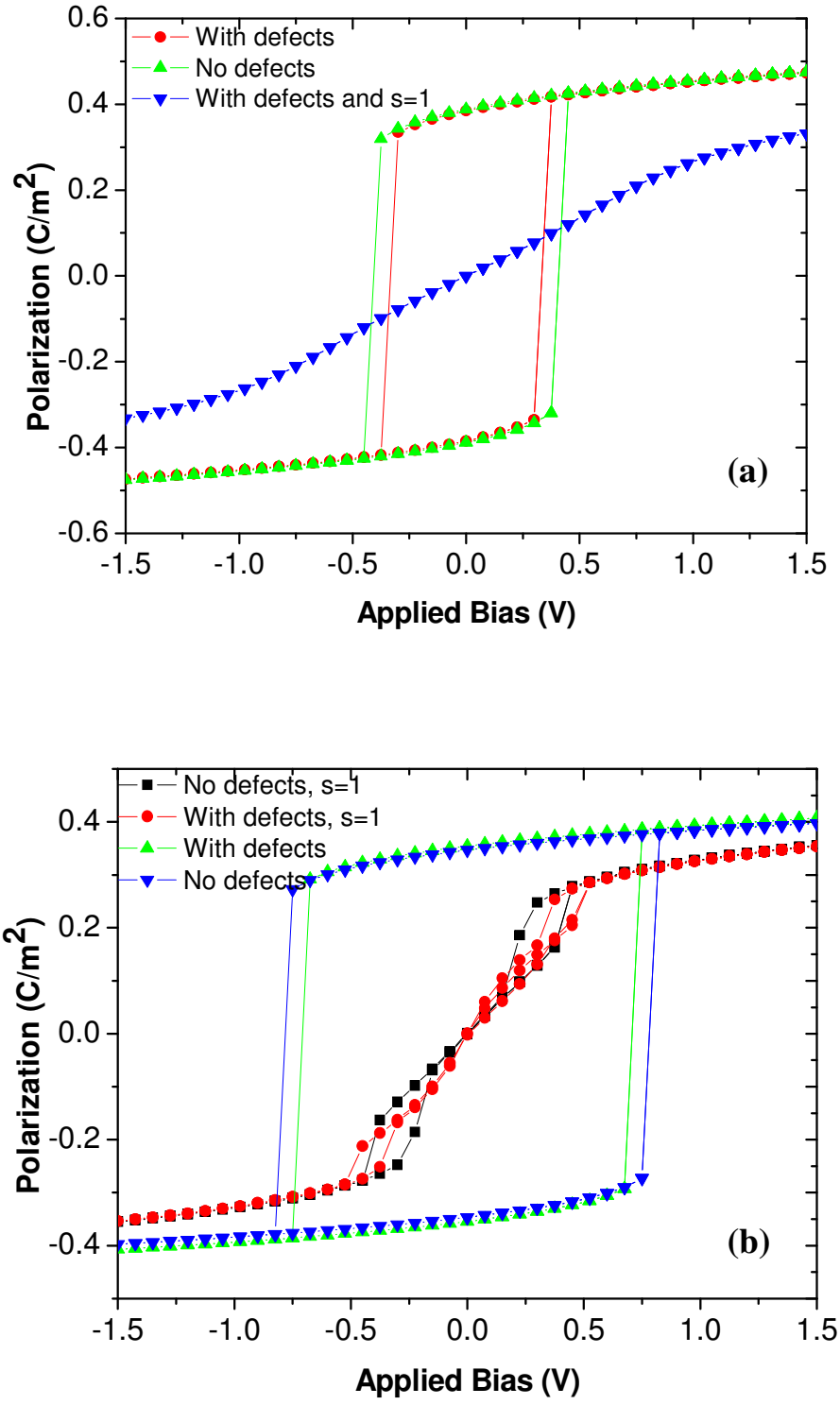

Figure 8. Misirlioglu *et al*.

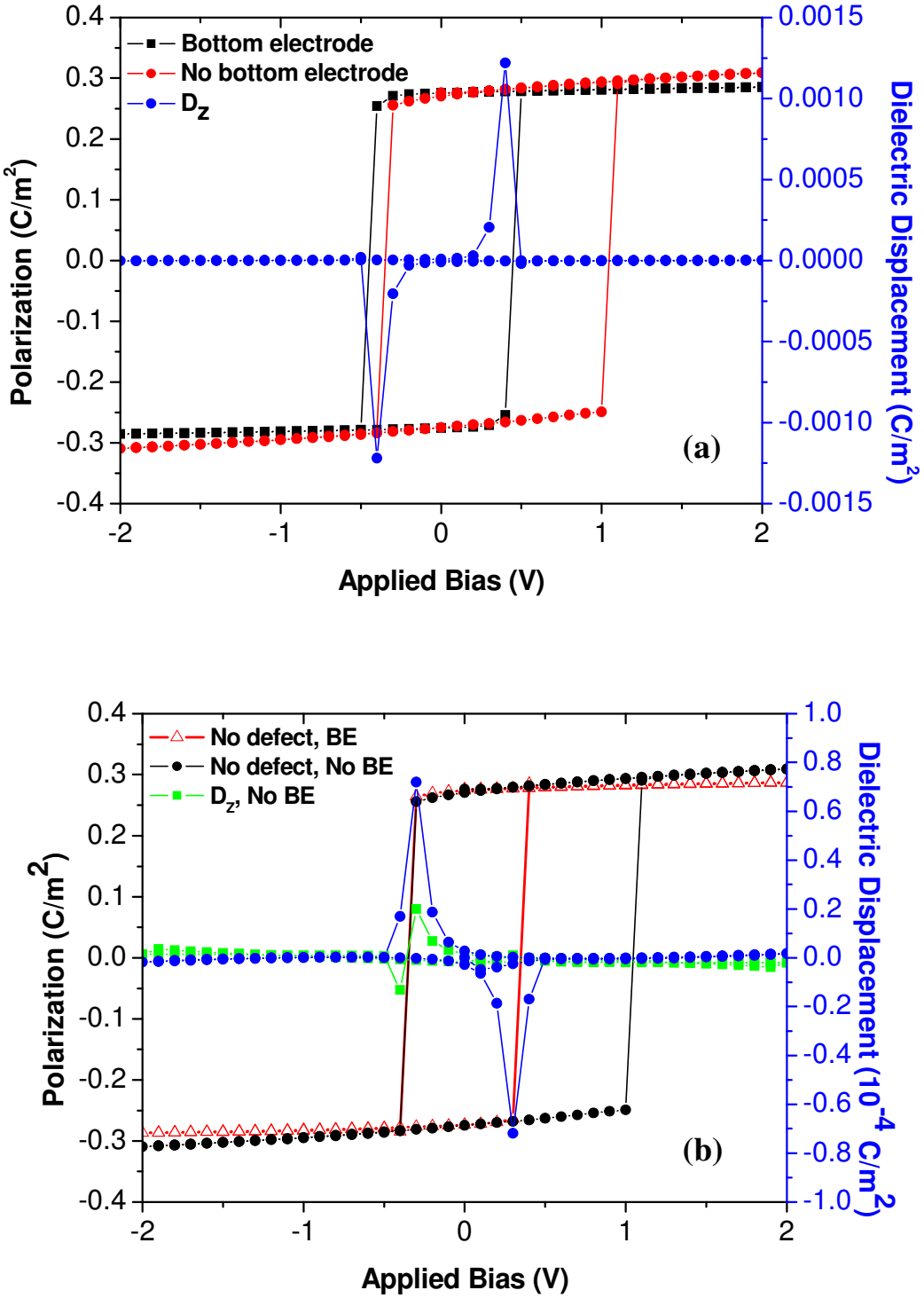

Figure 9. Misirlioglu *et al*.

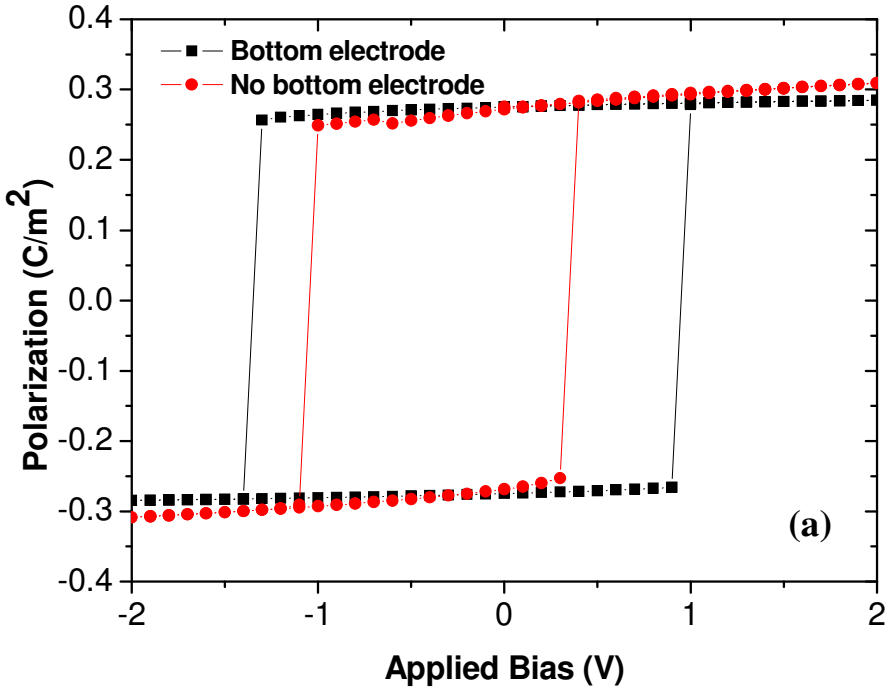

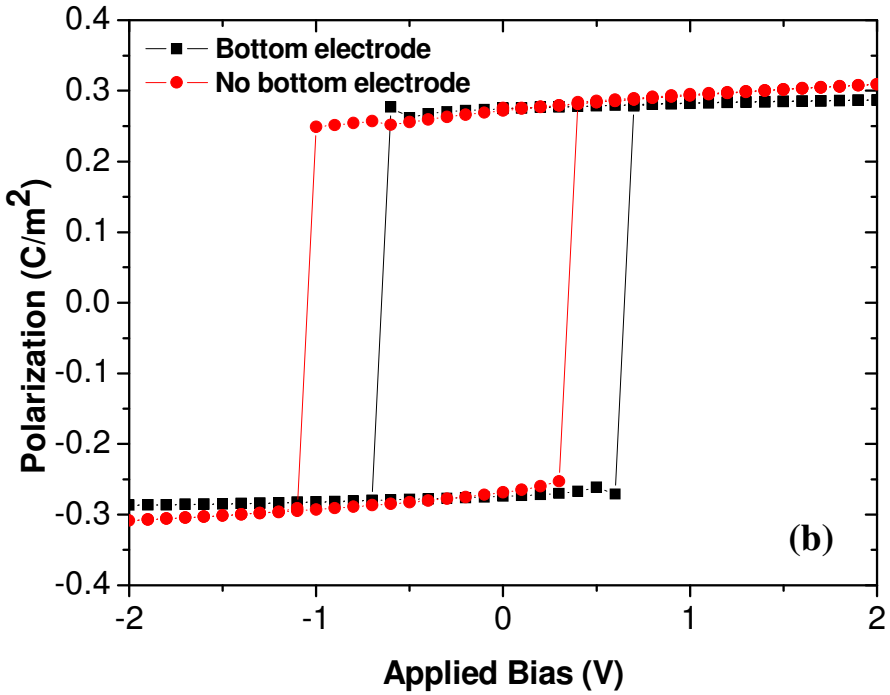

Figure 10. Misirlioglu *et al*.